Effect of Metal Environment and Immobilization on the Catalytic Activity of a Cu Superoxide Dismutase Mimic

Micaela Richezzi, Joaquín Ferreyra, Sharon Signorella, Claudia Palopoli, Gustavo Terrestre, Nora Pellegri, Christelle Hureau, Sandra R Signorella

inorganics

MDPI

Article

Effect of Metal Environment and Immobilization on the Catalytic Activity of a Cu Superoxide Dismutase Mimic

Micaela Richezzi [1], Joaquín Ferreyra [1], Sharon Signorella [1], Claudia Palopoli [1], Gustavo Terrestre [1], Nora Pellegri [2], Christelle Hureau [3] and Sandra R. Signorella [1,*]

[1] IQUIR (Instituto de Química Rosario), Consejo Nacional de Investigaciones Científicas y Técnicas (CONICET), Facultad de Ciencias Bioquímicas y Farmacéuticas, Universidad Nacional de Rosario, Suipacha 531, Rosario 2000, Argentina; richezzi@iquir-conicet.gov.ar (M.R.); ferreyra@iquir-conicet.gov.ar (J.F.); ssignorella@iquir-conicet.gov.ar (S.S.); palopoli@iquir-conicet.gov.ar (C.P.); terrestre@iquir-conicet.gov.ar (G.T.)

[2] IFIR (Instituto de Física Rosario), Consejo Nacional de Investigaciones Científicas y Técnicas (CONICET), Facultad de Ciencias Exactas, Ingeniería y Agrimensura, Universidad Nacional de Rosario, 27 de Febrero 210 bis, Rosario 2000, Argentina; pellegri@ifir-conicet.gov.ar

[3] LCC (Laboratoire de Chimie de Coordination) CNRS, Université de Toulouse, 205 Route de Narbonne, 31077 Toulouse, France; christelle.hureau@lcc-toulouse.fr

* Correspondence: signorella@iquir-conicet.gov.ar

Abstract: The Cu(II)/Cu(I) conversion involves variation in the coordination number and geometry around the metal center. Therefore, the flexibility/rigidity of the ligand plays a critical role in the design of copper superoxide dismutase (SOD) mimics. A 1,3-Bis[(pyridin-2-ylmethyl)(propargyl)amino]propane (pypapn), a flexible ligand with an N_4-donor set, was used to prepare [Cu(pypapn)$(ClO_4)_2$], a *trans*-Cu(II) complex whose structure was determined by the X-ray diffraction. In DMF or water, perchlorate anions are exchanged with solvent molecules, affording [Cu(pypan)$(solv)_2]^{2+}$ that catalyzes $O_2^{\bullet-}$ dismutation with a second-order rate constant k_{McF} = 1.26 × 10^7 M^{-1} s^{-1}, at pH 7.8. This high activity results from a combination of ligand flexibility, total charge, and labile binding sites, which places [Cu(pypapn)$(solv)_2]^{2+}$ above other mononuclear Cu(II) complexes with more favorable redox potentials. The covalent anchoring of the alkyne group of the complex to azide functionalized mesoporous silica through "click" chemistry resulted in the retention of the SOD activity and improved stability. A dicationic Cu(II)-N_4-Schiff base complex encapsulated in mesoporous silica was also tested as an SOD mimic, displaying higher activity than the free complex, although lower than [Cu(pypapn)$(solv)_2]^{2+}$. The robustness of covalently attached or encapsulated doubly charged Cu(II) complexes in a mesoporous matrix appears as a suitable approach for the design of copper-based hybrid catalysts for $O_2^{\bullet-}$ dismutation under physiological conditions.

Keywords: Cu-based SOD mimic; structure; mesoporous silica; click chemistry; SOD activity

Citation: Richezzi, M.; Ferreyra, J.; Signorella, S.; Palopoli, C.; Terrestre, G.; Pellegri, N.; Hureau, C.; Signorella, S.R. Effect of Metal Environment and Immobilization on the Catalytic Activity of a Cu Superoxide Dismutase Mimic. *Inorganics* **2023**, *11*, 425. https://doi.org/10.3390/inorganics11110425

Academic Editor: Vladimir Arion

Received: 7 October 2023
Revised: 17 October 2023
Accepted: 24 October 2023
Published: 27 October 2023

1. Introduction

Superoxide radical ($O_2^{\bullet-}$) is part of aerobic life. It is formed during the O_2 metabolism under normal physiological conditions and is the major initial form of other reactive oxygen species (ROS) associated with oxidative stress, such as H_2O_2 and $HO^{\bullet}$ radicals [1]. Superoxide dismutase (SOD) enzymes are efficient endogenous defenses that catalyze $O_2^{\bullet-}$ dismutation, regulating its concentration and keeping it at a tolerable level [2]. The imbalanced production of $O_2^{\bullet-}$ and other ROS associated with a number of neurodegenerative diseases [3] has stimulated the research of synthetic catalytic antioxidants to assist the endogenous counterparts in the suppression of ROS [4]. Among SOD enzymes, copper–zinc superoxide dismutase enzyme (CuZnSOD) catalyzes the proton-dependent dismutation of $O_2^{\bullet-}$ at a bimetallic site, where the copper ion is the redox partner of $O_2^{\bullet-}$, and Zn(II) plays a structural role in the enzyme stability [2,5]. In the active site of the

oxidized form of the enzyme, the Cu(II) ion is bound to the N_4-donor set of four histidine residues and one water molecule, adopting a distorted square–pyramidal geometry [6]. The Cu(II) ion is bridged to the Zn(II) ion through the imidazolate ring from one of the histidine residues, and the Zn(II) coordination sphere is completed by two histidine and one aspartate residues disposed in a distorted tetrahedral geometry (Figure 1) [5,6].

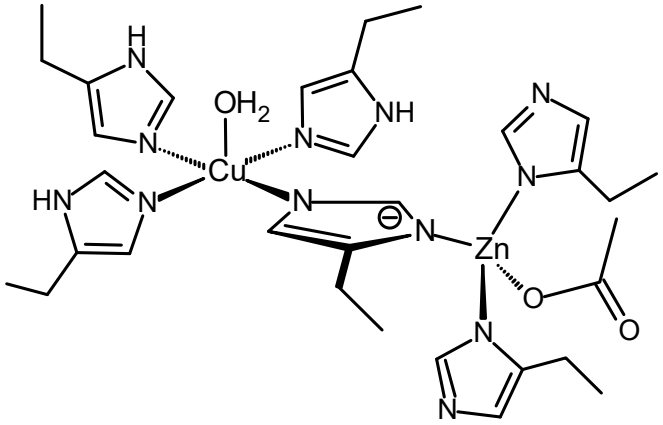

Figure 1. Active site of CuZnSOD.

In the search for efficient SOD mimics, a number of Cu(II) complexes with non-heme ligand scaffolds bearing an N_4-donor set have been synthesized and their SOD activity evaluated [7–17]. During the redox cycle, the switch between Cu(II) and Cu(I) oxidation states involves changes in coordination number and geometry around the metal ion, i.e., from tetragonal to tetrahedral [18,19]. Therefore, more flexible ligands can be thought to be better candidates to speed up electron transfer with a low reorganization energy barrier [20,21]. To serve as a therapeutic antioxidant, besides being active, the complex must be stable at physiological pH. However, in a solution, SOD mimics may undergo hydrolysis, metal dissociation, or oligomerization processes during the redox reaction [8,22,23]. Immobilization of a catalyst in a mesoporous solid has proven to be a good strategy for its protection and site isolation, improving its stability while preserving the properties of the homogeneous system [24–28]. Among the solid supports, mesoporous silica particles possess a large contact surface and pore volume, which allows for high catalyst loading [29,30], chemical and mechanical stability [31,32], biocompatibility [33], and controllable geometric parameters that enable a suitable design of different types and sizes of pores [29]. An effective approach to reducing the complex leaching from the silica consists of the covalent attachment of the catalyst to mesoporous silica employing "click" chemistry [34–37]. In this work, the SOD activity of the Cu(II) complex formed with an N_4-tetradentate "clickable" ligand, 1,3-bis[(pyridin-2-ylmethyl)(propargyl)amino]propane (pypapn, Scheme 1) [38], was evaluated in homogeneous phase and covalently grafted to azido functionalized mesoporous silicas, aimed at assessing the role played by this ligand on the catalytic activity and the effect of the covalent anchoring on the catalyst stability. Additionally, the SOD activity of the Cu(II) complex of *N*,*N*′-bis(2-pyridylmethylen)propane-1,3-diamine (py_2pn, Scheme 1), an N_4-Schiff base ligand, was evaluated after insertion in mesoporous silica by ionic exchange. Results obtained via employing these two immobilization approaches are compared with the intention to ascertain the effect of ionic vs. covalent binding of the catalyst on the support of the turnover numbers and catalyst recovery.

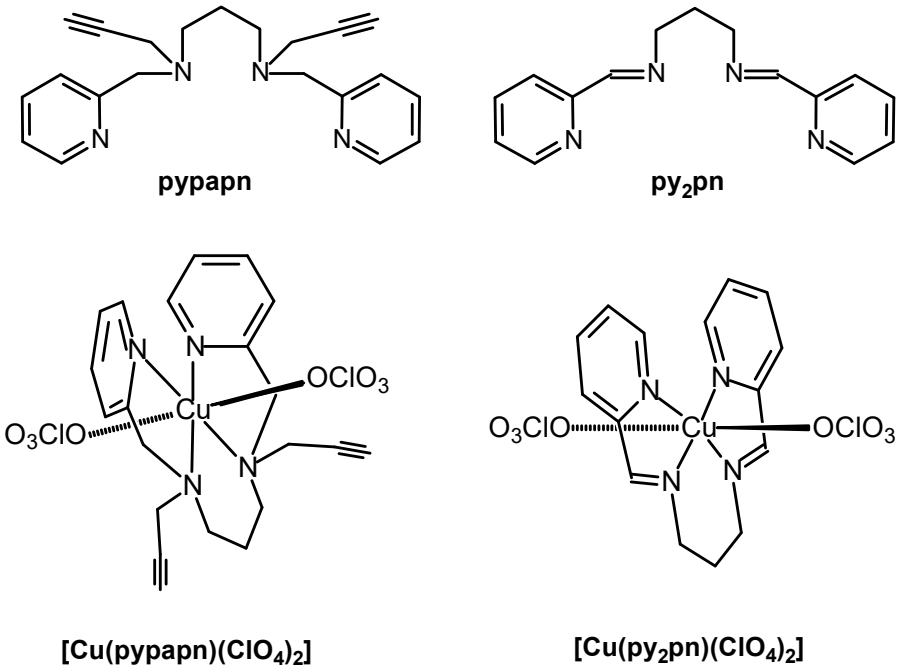

Scheme 1. Ligands and complexes used in this work.

2. Results

2.1. Characterization of the Complex

The reaction of equimolar amounts of pypapn and $Cu(OAc)_2$ in methanol at room temperature afforded a greenish–blue solution. Even when color changes were observed immediately after mixing, it was necessary to add sodium perchlorate and then hexane for the $[Cu(pypapn)(ClO_4)_2]$ complex to separate from the solution as a violet–blue polycrystalline solid. Single crystals of $[Cu(pypapn)(ClO_4)_2]$ could be obtained by slow diffusion of the reaction mixture into toluene at 4 °C. X-ray diffraction analysis revealed that the complex crystallizes in the orthorhombic F d d 2 space group with a lattice comprising discrete $[Cu(pypapn)(ClO_4)_2]$ molecules with Cu(II) bound to the tetradentate ligand and two perchlorate anions, as illustrated in Figure 2.

Bond distances and angles summarized in the caption of Figure 2 indicate that the coordination environment of the Cu(II) ion can be described as an elongated octahedron in which the equatorial plane is defined by the N_4-donor set of the pypapn ligand while the apical positions are occupied by two oxygen atoms belonging to two perchlorate anions. The Cu-O bond distances (2.620 Å) are significantly longer than the equatorial Cu-N ones (Cu-N_{py} 1.987 and Cu-N_{am} 2.057 Å), indicating that the perchlorate anions are weakly bound to the metal ion. The values of the dihedral angles around the Cu(II) center are between 82.28 and 99.53°, evidencing the deviation from an ideal octahedral geometry. In the crystal lattice of $[Cu(pypapn)(ClO_4)_2]$, the molecules are arranged in layers oriented parallel to the *bc* plane (Figure S1) and interconnected through H-bond contacts between the perchlorate O-atoms and the alkyne H-atom of a neighbor molecule, with H(C9)···O2 = 2.370 Å and H(C9)· · ·O4 = 3.187 Å distances. The long axes of the complex molecules in each layer are aligned on the crystallographic *a*-axis intercalated between molecules of adjacent layers.

The FT-IR spectrum of the complex (Figure 3a) displays intense absorption bands at 3262 and 2117 cm^{-1}, assigned to the ≡C-H and C≡C stretching vibrations of the terminal alkyne, and at 1118, 1067, and 622 cm^{-1}, corresponding to the perchlorate anions. Additionally, the shift of the strong in-plane C=N and C=C stretching vibrations of the pyridine ring from 1588 and 1437 cm^{-1} in the ligand to 1611 and 1445 cm^{-1} in the complex is a clear indication of the metal coordination to the N_{py} atom [39], in agreement with the crystal structure of the complex.

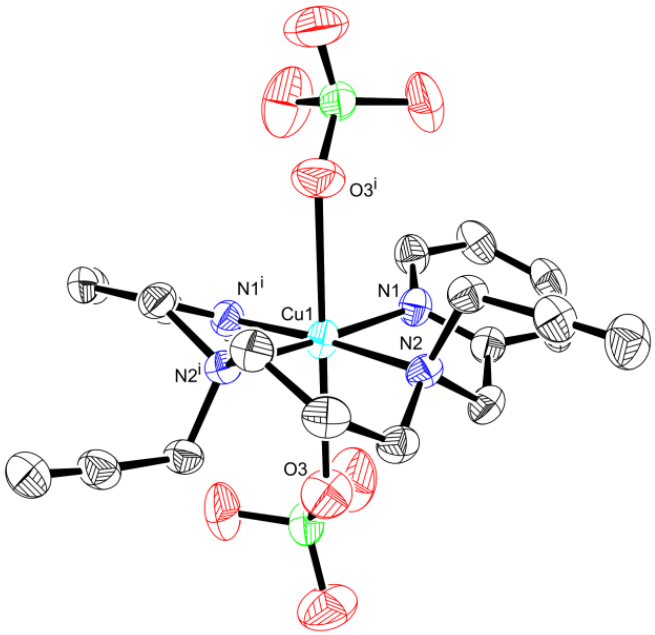

Figure 2. Molecular structure of complex [Cu(pypapn)(ClO_4)$_2$] at the 50% probability level with atom numbering. Selected bond lengths (Å) and angles (°): Cu1-N1 1.987(3); Cu1-N2 2.052(3); Cu1-O3 2.620(3); N1-Cu1-N1^{i} 99.53(19); N1-Cu1-N2^{i} 175.97(14); N1-Cu1-N2 82.28(10); N2-Cu1-N2^{i} 96.13(18); N1-Cu1-O3 91.53(13); N2-Cu1-O3 87.68(11); N1^{i}-Cu1-O3 88.67(12); N2^{i}-Cu1-O3 92.11(12); O3-Cu1-O3^{i} 179.69 (18). Standard deviations in parentheses. Symmetry transformations used to generate equivalent i atoms: −x + 1; −y + 1; z.

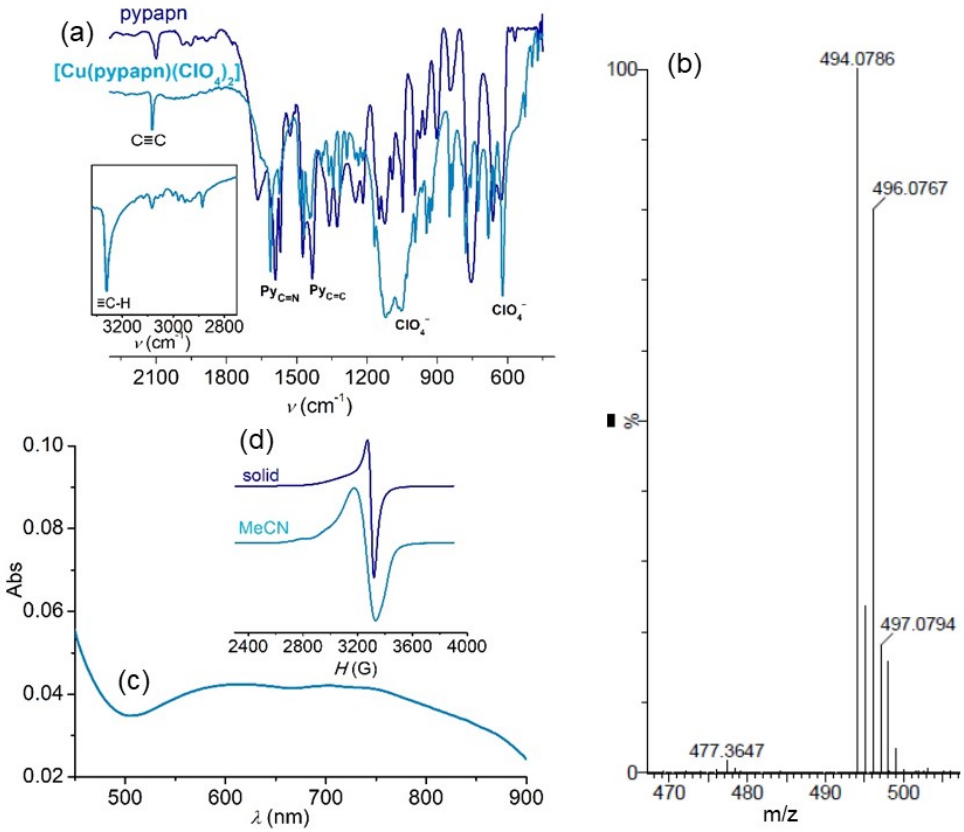

Figure 3. (**a**) FT-IR spectra of pypapn and [Cu(pypapn)(ClO_4)$_2$]. (**b**) HRMS of [Cu(pypapn)(ClO_4)]$^{+}$ in MeCN. (**c**) Electronic spectrum of 5 × 10^{-4} M [Cu(pypapn)(ClO_4)$_2$] in MeCN. (**d**) EPR spectra of powdered and frozen MeCN solution of [Cu(pypapn)(ClO_4)$_2$]; T = 120 K; ν = 9.51 GHz.

The chemical composition of the complex in solution was confirmed by the high-resolution mass spectrum (HRMS) of the complex in acetonitrile (Figure 3b) that shows the peak at m/z = 494.0786, corresponding to $[Cu(pypapn)(ClO_4)]^+$. The full ESI-mass spectrum (Figure S2) also shows peaks at m/z = 197.5634 (12%) and 395.1297 (11%) assigned to $[Cu(pypapn)]^{2+}$ and $[Cu(pypapn)]^+$, respectively, besides the peak of $[Cu(pypapn)(ClO_4)]^+$ (10%). These species are present in relatively low proportion compared to the peak at m/z = 440.1276 (100%), corresponding to the $[Cu(pypapn)(CHO_2)]^+$ monocation generated by perchlorate exchange with the formate anion present in the spectrometer. It is worth noting that the isotopic distribution of all the peaks is consistent with the simulated spectra. As expected, in the negative mode, the HRMS exhibits the peaks corresponding to the ClO_4^- anion (not shown).

The electronic spectrum of $[Cu(pypapn)(ClO_4)_2]$ in acetonitrile displays a low-intensity broad absorption band envelope centered at 653 nm (ε = 76 M^{-1} cm^{-1}), characteristic of the d–d transitions of Cu(II) in a tetragonal field. A detailed examination of this region of the spectrum shows that this band splits into two bands of similar intensity (Figure 3c), with energies of 14,184 cm^{-1} and 16,529 cm^{-1}, which can be assigned to $d_{z2} \rightarrow d_{x2\text{-}y2}$ and $d_{xz/yz} \rightarrow d_{x2\text{-}y2}$ transitions, respectively, consistent with an axially elongated octahedral geometry [18]. Other intense absorptions in the UV region (not shown) correspond to ligand-to-metal charge transfers (LMCT) overlapped with intraligand π-π* and n-π* transitions.

The X-band electron paramagnetic resonance (EPR) spectrum of powdered $[Cu(pypapn)(ClO_4)_2]$ shows an axial signal typical of Cu(II) sites in tetragonal geometry with $g_{\parallel}$ = 2.20 and $g_{\perp}$ = 2.06. The spectrum registered on a frozen acetonitrile solution of $[Cu(pypapn)(ClO_4)_2]$ (Figure 3d) is consistent with a $d_{x^2-y^2}$ ground state in a slightly distorted N_4-square–planar geometry, with spectral parameters $g_{\parallel}$ = 2.25 and $g_{\perp}$ = 2.08. In this solvent, the spectrum is broad [40], and only two of the four parallel hyperfine features are observed, from which the hyperfine coupling to the Cu nuclear spin $A_{\parallel} = 181 \times 10^{-4}$ cm^{-1} was estimated. Moreover, the empirical distortion index $f(g_{\parallel}/A_{\parallel})$ = 124 cm [41] indicates that in solution, the complex exhibits slight tetrahedral distortion from tetragonal geometry, in agreement with UV-vis results. In this poorly coordinating solvent (DN^{MeCN} = 14), the perchlorate anions remain bound to Cu(II), affording a neutral molecular complex. This was confirmed by the conductivity of the complex measured in acetonitrile, which shows non-electrolytic behavior (same conductivity as for the neat solvent). By contrast, in DMF, a more coordinating solvent (DN^{DMF} = 27), the molar conductivity of the complex is 132 Ω^{-1} cm^2 mol^{-1}, a value expected for a 1:2 electrolyte in this solvent [42]. Therefore, perchlorate is substituted by DMF to afford $[Cu(pypapn)(DMF)_2]^{2+}$. The coordination of DMF is also supported by the bathochromic shift of the d–d transition in the visible spectrum, with a broad band centered at ~750 nm as the axial positions are occupied by DMF, lowering the energy of the transition along the z-axis (Figure S3).

The ^1H NMR paramagnetic spectrum of $[Cu(pypapn)(ClO_4)_2]$ in CD_3CN (Figure 4a) shows that the pyridine protons undergo broadening as well as a differential isotropic shift depending on the distance between each proton and the metal center. The broad signal at the low field can be assigned to overlapped H_α/H_α' at 11.0 ppm, with a peak width of 104 Hz. Meanwhile, the β/β' and γ pyridine protons can be observed at 8.61, 7.95, and 7.48 ppm, displaying signals with a peak width of 20 Hz, 24 Hz, and 32 Hz, respectively. This spectral pattern suggests that the two pyridine rings are symmetrically related around the copper center, which is in agreement with the elongated tetragonal geometry proposed from the EPR spectrum of the complex in this solvent. Moreover, signals belonging to the methylene protons broaden and split in the 2.5–4.0 ppm spectral region, with peak widths in the range from 12 to 32 Hz, depending on their relative location. Integration affords an 8:6 ratio for the pyridine and methylene protons adjacent to the donor *N* atoms, so it is possible that resonances originating from methylene protons

closest to the Cu(II) ion are broadened and shifted downfield. The broad resonance at ~13 ppm can account for this (Inset in Figure 4a).

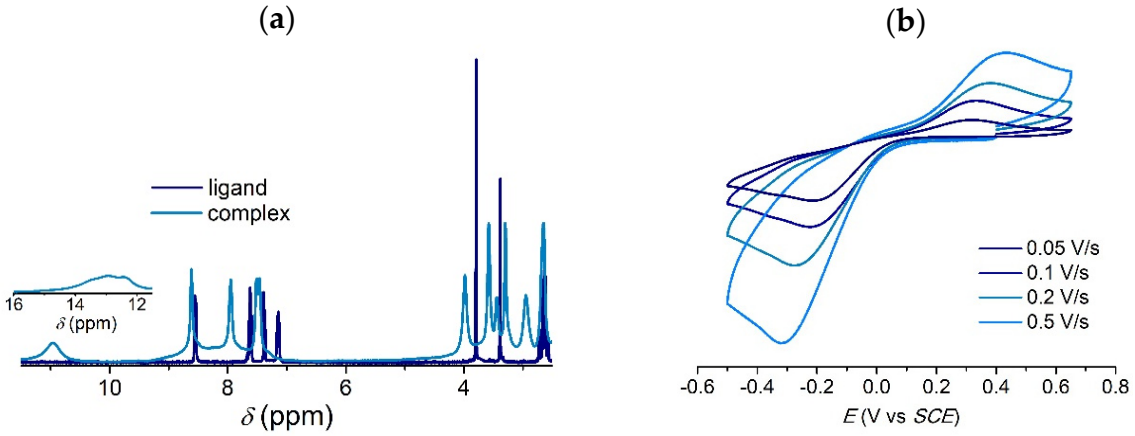

Figure 4. (**a**) ^{1}H NMR spectrum of [Cu(pypapn)$(ClO_4)_2$] in CD_3CN. (**b**) Cyclic voltammogram of 1 mM [Cu(pypapn)$(ClO_4)_2$] in acetonitrile, 0.1 M Bu_4NPF_6, and glassy C/Pt/SCE, at different scan rates.

The donor sites, the geometry, and the flexibility of the ligand are known to modulate the redox behavior of the copper center and, consequently, its reactivity toward superoxide. The redox potential of [Cu(pypapn)$(ClO_4)_2$] was determined by cyclic voltammetry. The voltammograms of the complex in acetonitrile at various scan rates (Figure 4b) show the growth of the intensity of the cathodic and anodic peaks as the rate increases, along with a shift of both peaks to more negative and more positive potentials, respectively. The ΔE value (0.55 V at υ = 0.1 V/s), its dependence on υ, and the I_{pa}/I_{pc} ratio of 0.35 indicate that the reduction in the complex is irreversible and takes place at E_{pc} = −0.22 V vs. *SCE* (υ = 0.1 V/s), while the oxidation of the reduced complex occurs at E_{pa} = 0.33 V vs. *SCE*. The irreversibility of the process can be attributed to geometry changes experienced by the complex during reduction. Most probably, the reduction in the tetragonal Cu(II) complex is accompanied by perchlorate dissociation to yield Cu(I) in a flattened tetrahedral geometry, and the observed oxidation peak originates from this four-coordinate complex. It must be noted that the absence of a re-dissolution peak upon anodic polarization scans indicates that no copper is released from the Cu(I) complex generated at the electrode. For comparison, $[Cu(py_2pn)]^{2+}$, formed with the Schiff base *N*,*N*′-bis(2-pyridylmethylen)propane-1,3-diamine, is reduced at −0.044 V vs. SCE [7]. Therefore, the more flexible N_4-diamine/dipyridine ligand stabilizes Cu(II) toward reduction better than the N_4-diimine/dipyridine one, reflecting the higher electron–donor ability of pypapn.

2.2. Synthesis and Characterization of Modified Mesoporous Silicas

2.2.1. Synthesis of Cu-pypntriazole@SBA-15 and Cu-pypntriazole@OP-MS

The $[Cu(pypapn)(solv)_2]^{2+}$ complex was covalently anchored to mesoporous silica matrix by reaction of the alkynyl groups with azide functionalized mesoporous silica employing "click" chemistry. Two different approaches were used to prepare the azide-modified mesoporous silica: post-synthetic functionalization of SBA-15 silica; and a co-condensation method [28]. The first method consists of grafting (3-bromopropyl)trichlorosilane to SBA-15 mesoporous silica to yield Brpn@SBA-15, followed by the bromine substitution by azide to afford N_3pn@SBA-15 (Scheme 2, route (a)). The other procedure involves a "one-pot" co-condensation reaction using tetraethyl orthosilicate (TEOS) and 3-azidopropyltriethoxysilane (AzPTES) in the presence of the triblock copolymer Pluronic P-123 as surfactant template (Scheme 2, route (b)). In the one-pot methodology, the azidopropyl chains are placed between the copolymer chains favoring the binding of the organic groups to the inner pore

walls of the silica particles [43,44]. The material obtained by this procedure exhibits textural properties similar to SBA-15 (see below). Subsequently, the pypapn ligand was covalently linked to the two azide functionalized silicas by the formation of the 1,2,3-triazole ring, using $(Ph_3P)_3CuBr$ as a catalyst, to afford pypntriazole@SBA-15 and pypntriazole@OP-MS. In each case, the reaction was stopped after the disappearance of the azide band in the ATR-FTIR spectra of the solid samples. The Cu(II) complex was formed in situ by the addition of a solution of $Cu(ClO_4)_2$ to a suspension of pypntriazole@SBA-15 or pypntriazole@OP-MS in methanol, yielding Cu-pypntriazole@SBA-15 and Cu-pypntriazole@OP-MS, with similar Cu(II) loading, as described in the experimental part. In both hybrid materials, the ligand is attached to the channel walls at a single binding site (Scheme 2), as evidenced by metal and nitrogen analyses.

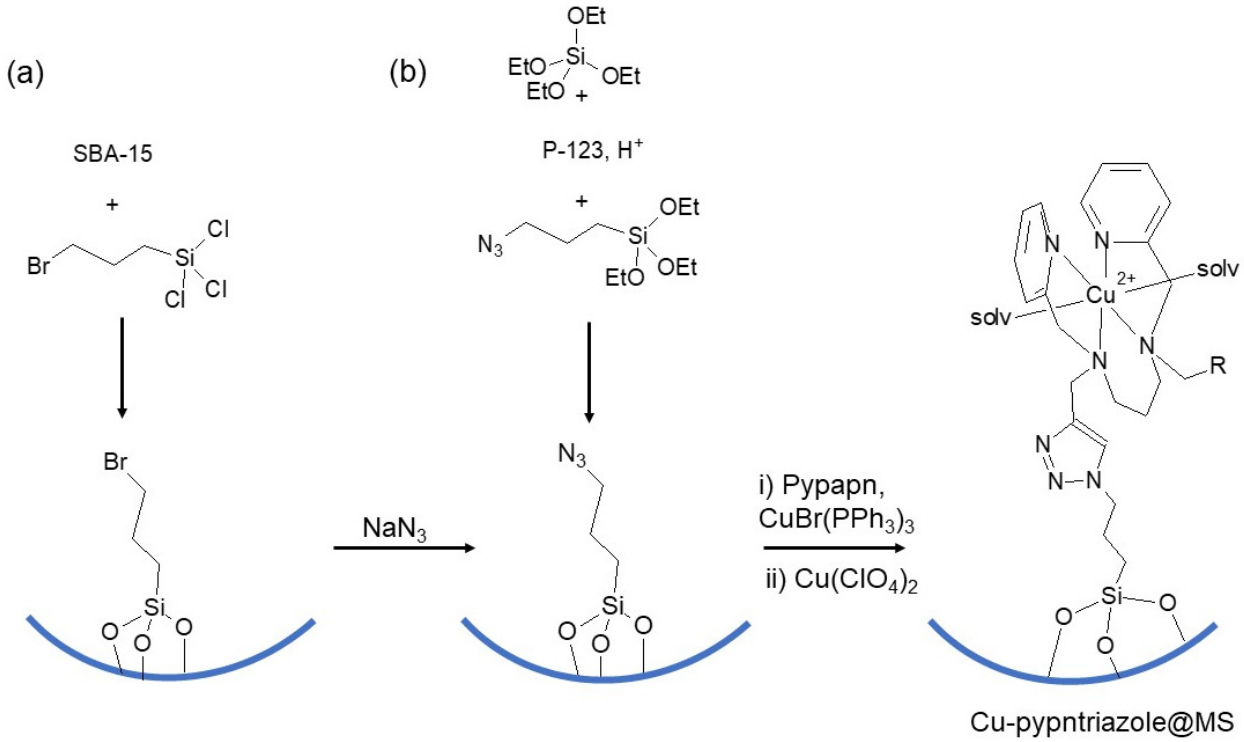

Scheme 2. Synthetic routes toward the hybrid catalyst. MS = SBA-15 or OP-MS.

For comparative purposes, the complex $[Cu(py_2pn)]^{2+}$ formed with the N_4-Schiff-base was introduced into the mesoporous matrix of SBA-15 silica by ionic exchange, affording the Cu-py_2pn@SBA-15 hybrid material where the divalent complex cation was retained inside the silica channels by electrostatic interaction with the silanolate groups of the pores' surfaces. The FT-IR spectrum of the material confirms that the complex is essentially located inside the pores since it shows only the strong bands of the Si-O-Si, Si-OH_2, and Si-OH groups but no or negligible bands belonging to the functional groups of the Schiff-base. The lower proportion of the encapsulated complex in SBA-15 agrees with the smaller decrease in the pore volume and surface area (see below) determined from the adsorption N_2 isotherms of this complex compared to Cu-pypntriazole@SBA-15.

2.2.2. Textural Properties and Morphology of the Mesoporous Materials

SBA-15, prepared following a reported methodology [11], shows an ordered mesostructure with a high specific surface area and pore width of 4.9 nm (Table 1) suitable to host the catalysts, which are around 1.0 nm wide (calculated from the crystal structures of $[Cu(pypapn)(ClO_4)_2]$ and $[Cu(py_2pn)(ClO_4)_2]$ [7]).

Table 1. Textural characterization of mesoporous materials.

	S_{BET} (m^2 g^{-1})	$V_{\mu P}$ (cm^3 g^{-1})	V_{MP} (cm^3 g^{-1})	V_{TP} (cm^3 g^{-1})	w_P (nm)	mmol Complex/ 100 g Material
SBA-15	641	0.03	0.64	0.79	4.9	-
Cu-pypntriazole@SBA-15	310	0.00	0.34	0.41	3.7	24
Cu-py_2pn@SBA-15	501	0.00	0.57	0.71	4.4	9.8
N_3pn@OP-MS	362	0.00	0.41	0.47	4.8	-
Cu-pypntriazole@OP-MS	433	0.00	0.40	0.46	4.0	18

$V_{TP} = V_{mP} + V_{primary\ MP} + V_{secondary\ MP}$. MP = mesopore. µP = micropore. w_p = pore diameter.

All the materials obtained by catalyst covalent grafting or encapsulation display type IV isotherms with a sharp jump and an H1 hysteresis loop at relative pressure p/p° = 0.55–0.75 (Figure 5). This behavior is typical of ordered mesoporous materials, denoting that the hybrids possess mesostructure similar to SBA-15 and uniform distribution of pore sizes, although smaller pore volume and surface area (Table 1) as a consequence of the presence of the organic groups or catalyst inside the channels.

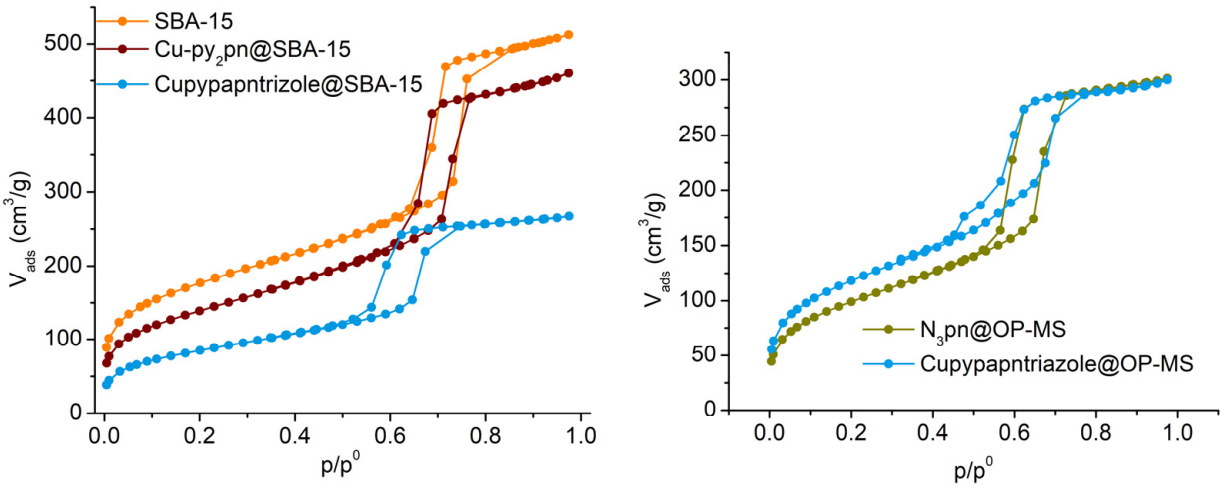

Figure 5. Adsorption–desorption N_2 isotherms of mesoporous materials.

The morphology and size of the mesoporous silica particles were analyzed by scanning electron microscopy (SEM, Figure S4). The SBA-15 particles are oblong, with an average size of ~1–1.5 µm long, lined up forming chains of 30–50 µm long. The hybrid materials obtained by either covalent attachment or encapsulation of the catalyst in SBA-15 maintain the morphology of the starting silica particles, although they align to form shorter chains of 15–20 µm long. Fiber-like mesoporous N_3pn@OP-MS is made up of a bundle of wires forming long strands of 50–100 µm long, and after the "click" reaction, exhibits a similar morphology. Upon Cu binding, the hybrid catalyst shows rod-shaped particles of 2–3 µm long, forming wheatlike aggregates of 10–15 µm long.

Transmission electron microscopy (TEM) images of the three hybrid materials (Figure 6) corroborate the regular array of cylindrical channels, as well as the hexagonal pore arrangement, confirming a highly ordered mesostructure. The images show that the channels are oriented along the long axis of the particles and that the pore network reaches the particle surface, serving as a substrate entrance channel to interact with the catalyst. From statistical analysis of TEM images of Cu-pypntriazole@SBA-15, pore diameter and wall thickness were calculated using a protocol that takes into account integration over grey scales in carefully selected zones where the electron beam was perpendicular to the channels. The average pore diameter and wall thickness calculated in this way are 3.5 ± 0.6 nm and 4.7 ± 0.5 nm, respectively, in agreement with the pore size calculated from the adsorption isotherm. The histograms are shown in Figure S5.

These thick walls reflect the hydrothermal stability of the mesostructured silica particles without enlargement of the pore size and confer robustness to the catalytic material.

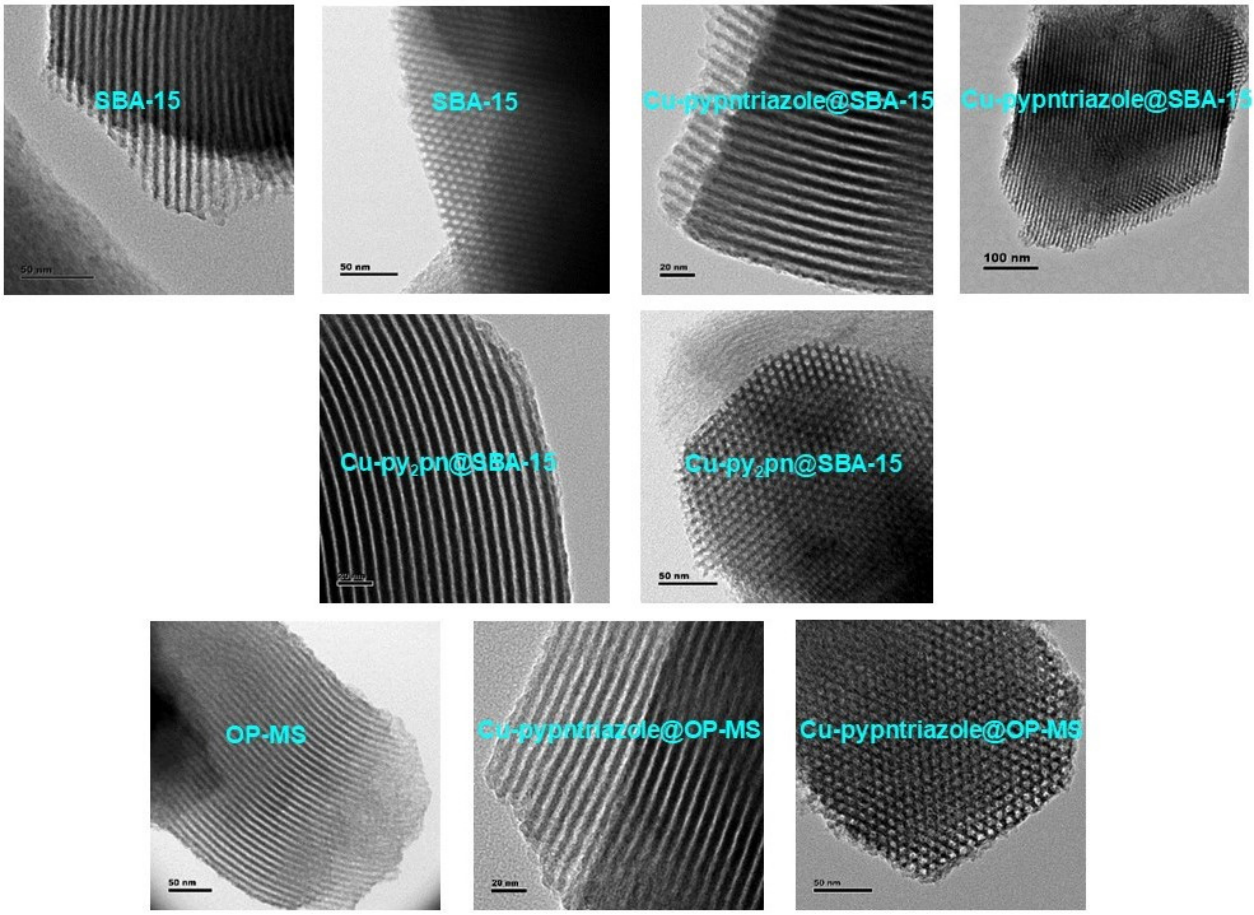

Figure 6. TEM images of hybrid materials showing the parallel channels and their hexagonal arrangement.

The ordered mesostructure of SBA-15 and Cu-pypntriazole@SBA-15 was also verified by low-angle X-ray diffraction (XRD, Figure S6). The XRD pattern indicates that SBA-15 exhibits a long-range mesoscopic ordering of hexagonal p6mm phases, as evidenced by the intense (100) peak and the weaker (110) and (200) reflections [45]. The observed pattern is not modified after anchoring the complex, confirming that the integrity of the porous structure is maintained. The peak at 2θ = 0.93 is not shifted after covalent attachment, but it shows a 25% decrease, as well as the higher order reflections, possibly due to a decrease in periodicity [46].

2.3. SOD Activity Studies

The SOD activity of the complex and the hybrid materials was measured in a phosphate buffer of pH 7.8. As described before, when $[Cu(pypapn)(ClO_4)_2]$ dissolves in MeCN, perchlorate anions remain coordinated to Cu(II), but when it is dissolved in a stronger donor solvent like DMF or water, ligand exchange occurs, and perchlorate is replaced by solvent molecules affording the dicationic $[Cu(pypapn)(solv)_2]^{2+}$ complex. For simplicity, hereafter, the solvated complex will be referred to as $[Cu(pypapn)]^{2+}$. Given the low solubility of the complex in aqueous phosphate buffer, it was first dissolved in DMF, and an aliquot of the concentrated solution was diluted with phosphate buffer of pH 7.8 to a final volume of 3.2 mL. In this way, complete dissolution of the complex was achieved, and the stability was verified by monitoring its electronic spectrum for 2 h. Spectra taken at different times after preparing the solution exhibited analogous absorption features and band intensities (Figure 7a). The stability of the hybrid materials was also checked after

incubation in a phosphate buffer of pH 7.8 for 2 h, followed by centrifugation and record of the UV-vis spectra of the supernatant. These measurements denoted the absence of complex released into the solution. The SOD activity of $[Cu(pypapn)]^{2+}$ and the hybrid materials was determined by the Beauchamps and Fridovich indirect assay using the NBT reagent [47] at pH 7.8. This assay is based on kinetic competition between NBT and the catalyst for photogenerated superoxide. Therefore, the SOD activity of the catalyst is measured by its ability to inhibit the formation of formazan, the product of the reaction of NBT with superoxide, observed at 560 nm. $[Cu(pypapn)]^{2+}$ displays activity, as shown in Figure 7b. The IC_{50} value, the concentration of catalyst that inhibits by 50% the NBT reduction by $O_2^{\bullet-}$, was determined from the plot of % inhibition vs. [catalyst] and used to calculate the McCord–Fridovich rate constant, k_{McF}, which is independent of the detector [48].

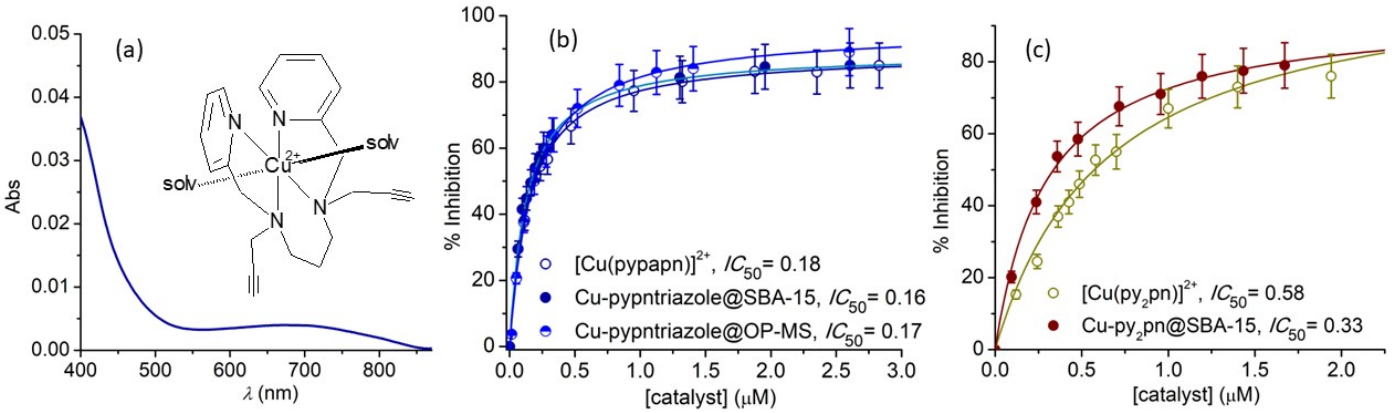

Figure 7. (**a**) UV-vis spectrum of 5×10^{-5} M $[Cu(pypapn)]^{2+}$ in buffer phosphate of pH = 7.8. SOD activity of (**b**) free and covalently attached $[Cu(pypapn)]^{2+}$ and (**c**) free and encapsulated $[Cu(py_2pn)]^{2+}$.

Table 2 lists the values of k_{McF} and $E_{1/2}$ (or E_p) redox potential for $[Cu(pypapn)]^{2+}$ and other reported Cu(II) complexes with open-chain ligands (see Chart S1 for their structures) [9–13,49,50]. If the catalyzed $O_2^{\bullet-}$ dismutation occurs through an outer sphere mechanism, a complex will be thermodynamically competent as a catalyst when its redox potential lies between the $E(O_2^{\bullet-}/H_2O_2) = 0.642$ V and $E(O_2/O_2^{\bullet-}) = -0.404$ V vs. SCE redox couples, at pH 7 [51]. On this basis, the best catalysts should be those with a metal-centered redox couple close to 0.12 V vs. *SCE* (pH 7), the midpoint between the oxidation and reduction in $O_2^{\bullet-}$ radical. However, in Table 2, it can be observed that $[Cu(MPBMPA)Cl]^{+}$ ($E_{pc} = -0.47$ V) is twice as active as $[Cu(pypapn)]^{2+}$ ($E_{pc} = -0.22$ V), even when its redox potential is outside the range for $O_2^{\bullet-}$ dismutation (entries 2,3, Table 2). Furthermore, $[Cu(pypapn)]^{2+}$ exhibits an SOD activity better than $[Cu(py_2pn)]^{2+}$ ($E_{1/2} = -0.044$ V) and similar to [Cu(PBMPA)Cl] ($E_{1/2} = 0.213$ V), although its redox potential is further away from 0.12 V (entries 3,4,7, Table 2). This behavior can be explained if the reaction takes place through an inner sphere mechanism where the redox potential is not the only relevant factor but also the flexibility of the ligand, steric hindrance, labile coordination sites, and the total charge of the complex. During catalysis, the coordination sphere of Cu in $[Cu(pypapn)]^{2+}$ must change between the tetragonal geometry of Cu(II) to the tetrahedral or tricoordinate geometry preferred by Cu(I). Although both $[Cu(pypapn)]^{2+}$ and $[Cu(py_2pn)]^{2+}$ have a similar geometrical arrangement of the N_4-tetradentate ligand around the Cu(II) ion, the diamine pypapn ligand is more flexible than the diimine py_2pn and adapts better to the geometrical reorganization required to accommodate the two metal oxidation states during catalysis. This is particularly evident for $[Cu(PuPy)]^{2+}$ (entry 1, Table 2) with a longer and more flexible tetramethylene chain between the imine groups that doubles the SOD activity of $[Cu(pypapn)]^{2+}$. The relevance of steric factors is evident in the four-time decrease in the SOD activity going from $[Cu(PuPy)]^{2+}$ to $[Cu(Pu\text{-}6\text{-}MePy)(H_2O)]^{2+}$, where the *o*-methyl substituted pyridine derivative hinders the access of $O_2^{\bullet-}$ to the metal center

(entries 1,6, Table 2). The number of labile positions available for binding the substrate via ligand exchange is a factor made evident when comparing [Cu(MPBMPA)Cl_2] and [Cu(PBMPA)Cl], the first being twice as active as the second (entries 2,4, Table 2). Another example is [CuZn(dien)$_2$(μ-Im)](ClO_4)$_3$, which during catalysis, dissociates, converting into [Cu(dien)]$^{2+}$, which can bind $O_2^{\bullet-}$ and promote its dismutation despite its very unfavorable redox potential (entry 5, Table 2). Although with similar ligand flexibility, the SOD activity of [Cu(PBMPA)Cl] is three times higher than that of the related complex [Cu(PClNOL)Cl]$^+$ (entries 4,8, Table 2), probably as a result of the combination of a more favorable redox potential of [Cu(PBMPA)Cl] and a stronger labilizing effect of the carboxylate compared to the alcohol group of [Cu(PClNOL)Cl]$^+$, to facilitate ligand exchange. The more rigid and planar Cu(II) complexes derived from salen and salpn ligands are the least active (entries 9–11, Table 2), even slower than Cu(ClO_4)$_2$ (k_{McF} = 2.7 × 10^6 M^{-1} s^{-1}) [52]; hence, reinforcing the ligand flexibility is a key factor in the $O_2^{\bullet-}$ dismutation catalyzed by the Cu(II) complexes.

Table 2. SOD activity of [Cu(pypapn)]$^{2+}$ and other functional SOD models.

Entry	Catalyst	Ligand Donor Sites	k_{McF} (10^6 M^{-1} s^{-1})	$E_{1/2}$ (V vs. SCE)	Ref.
1	[Cu(PuPy)]$^{2+}$	N_4	23.6	-	[9]
2	[Cu(MPBMPA)Cl_2]	N_3	21.2	−0.471	[10]
3	[Cu(pypapn)]$^{2+}$	N_4	12.6	−0.22 (E_{pc})	This work
4	[Cu(PBMPA)Cl]	N_3O	12.5	0.213	[10]
5	[CuZn(dien)$_2$(μ-Im)(ClO_4)$_2$]$^+$	N_3N_{Im}	6.46	−0.89 (E_{pc})	[11]
6	[Cu(Pu-6-MePy)(H_2O)]$^{2+}$	N_4	6.3	-	[12]
7	[Cu(py$_2$pn)]$^{2+}$	N_4	4.05	−0.044	[7]
8	[Cu(PClNOL)Cl]$^+$	N_3O	3.3	−0.416	[13]
9	[Cu(5-EtO-salpn)$ZnCl_2$]	N_2O_2	2.1	-	[49]
10	[Cu(4-OMe-salchda)$ZnCl_2$]	N_2O_2	0.87	-	[50]
11	[salpnCuZnCl_2]	N_2O_2	0.85	−0.689	[11]
12	CuZnSOD	N_4	2000	0.156	[2]
	Immobilized Catalyst		**k_{McF} (10^6 M^{-1} s^{-1})**		
13	Cu-pypntriazole@SBA-15		14.2		
14	Cu-pypntriazole@OP-MS		13.3		
15	Cu-py$_2$pn@SBA-15		6.9		

PuPy = N,N′-bis(2-pyridylmethylen)-1,4-butanediamine; HPBMPA, N-propanoate-*N*,*N*-bis-(2-pyridylmethyl)amine; dien = diethylenetriamine; HIm = imidazole; Pu-6-MePy = N,N′-bis(2-(6-methylpyridyl)methylen)-1,4-butanediamine; HPClNOL, 1-[bis(pyridin-2-ylmethyl)amino]-3-chloropropan-2-ol; salpn, 1,3-bis(salicylidenamino)propane; 4-OMe-salchda = N,N′-bis(4-methoxysalicylidene)cyclohexane-1,2-diamine.

Even the more flexible and active complexes listed in Table 2 are two orders of magnitude less active than the CuZnSOD enzyme (entry 12, Table 2), where the protein matrix constraints the metal geometry halfway between that of each oxidation state and the small structural reorganization is required for switching between the oxidized and reduced forms of the enzyme results in fast electron transfer.

Aimed at examining the effect of immobilization on the SOD activity and stability of the catalyst, the reactivity of the three hybrid materials toward $O_2^{\bullet-}$ was evaluated (Figure 7b,c). Cu-pypntriazole@SBA-15 and Cu-pypntriazole@OP-MS, with the catalyst covalently attached to the surface of the silica channels, retain the activity of the free complex (entries 13,14, Table 2). This result suggests that the ligand binding through the triazole does not restrain the ligand flexibility or affect the geometry of the metal center. Low-temperature X-band EPR spectra registered after the reaction of these hybrids with an excess of KO_2 in DMSO (shown for Cu-pypntriazole@SBA-15 in Figure 8a) confirmed that the immobilized complex keeps the geometrical arrangement of the ligand around the Cu(II) ion. The spectral parameters for Cu-pypntriazole@SBA-15 after

reaction with KO_2 are $g_{\|}$ = 2.25, $g_{\perp}$ = 2.06, $A_{\|}$ = 186 × 10^{-4} cm^{-1} and $f(g_{\|}/A_{\|})$ = 121 cm, denoting that Cu(II) is in a slightly distorted tetragonal geometry, similar to that observed for the complex in a homogeneous phase (Figure 8a). Interestingly, encapsulation of $[Cu(py_2pn)]^{2+}$ inside the SBA-15 silica matrix almost doubles the SOD activity of the free complex (entry 15, Table 2), probably because the silanolate–copper interaction renders the copper center more electrophilic, favoring electron transfer from $O_2^{\bullet-}$ to Cu(II). Also, in this case, the low-temperature X-band EPR spectrum registered after the reaction of Cu-py_2pn@SBA-15 with an excess of KO_2 in DMSO (Figure 8b) accounts for the retention of the complex structure in the silica pores. The calculated spectral parameters of Cu-py_2pn@SBA-15 are $g_{\|}$ = 2.23, $g_{\perp}$ = 2.05, $A_{\|}$ = 182 × 10^{-4} cm^{-1}, and $f(g_{\|}/A_{\|})$ = 123 cm, analogous to those of the complex in frozen DMSO solution [7]. It must be noted that the absence of the superoxide signal ($g_{\|}$ = 2.1021, $g_{\perp}$ = 2.003) [53] in the EPR spectra recorded after the reaction of the hybrids with 10-times excess of KO_2 in DMSO indicates that these materials act as catalysts for $O_2^{\bullet-}$ dismutation. Aimed at verifying if the SOD activity is retained after several cycles, the NBT conversion was measured with and without the hybrid material after consecutive illuminations of the reaction mixture. In each new illumination, the NBT concentration was kept constant by the addition of the required quantity of NBT to restore the starting concentration. Cu-pypntriazole@SBA-15, Cu-pypntriazole@OP-MS, and Cu-py_2pn@SBA-15 retain the activity after several illumination cycles, indicating that, in all cases, immobilization of the catalyst in the mesoporous matrix isolates and protects the complex to react with $O_2^{\bullet-}$, extending the catalyst life and reusability.

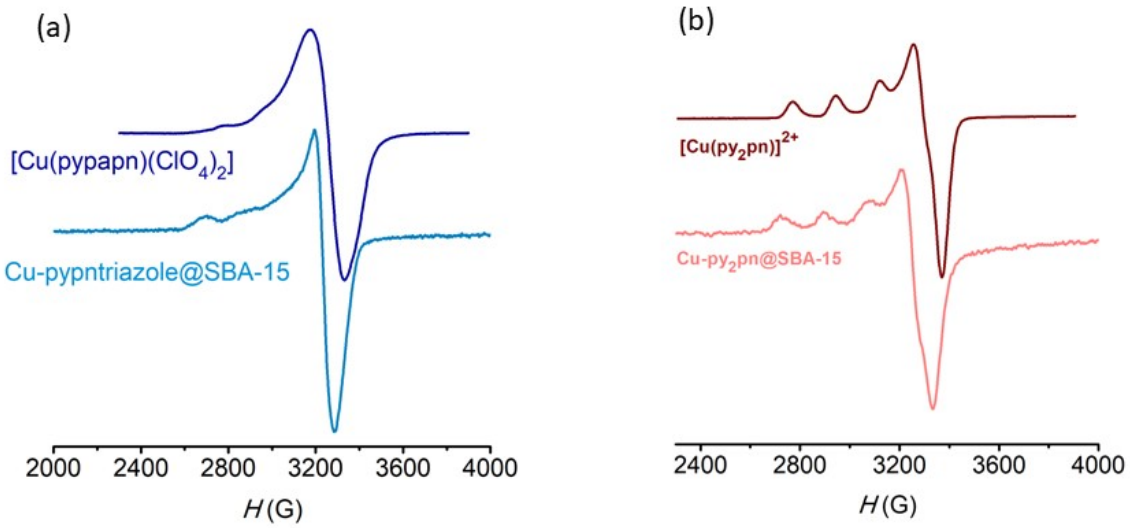

Figure 8. X-band EPR spectra of (**a**) $[Cu(pypapn)(ClO_4)_2]$ in frozen MeCN solution (ν = 9.5 GHz) and solid Cu-pypntriazole@SBA-15 (ν = 9.31 GHz). (**b**) $[Cu(py_2pn)]^{2+}$ in frozen DMSO solution (ν = 9.5 GHz) and solid Cu-py_2pn@SBA-15 (ν = 9.31 GHz). T = 120 K.

3. Materials and Methods

In this study, all the used reagents and solvents were commercial products of the highest available purity and, when necessary, were further purified via conventional methods.

3.1. Synthesis of Ligands, Complexes, and Hybrid Materials

The synthesis of the ligands N,N′-bis(2-pyridylmethylen)propane-1,3-diamine (py_2pn) [54] and 1,3-bis[(2-pyridilmethyl)(propargyl)amino]propane (pypapn) [38] and the complex $[Cu(py_2pn)(ClO_4)_2]$ [7] were described in previous papers.

3.1.1. Synthesis of [Cu(pypapn)(ClO_4)$_2$]

$Cu(OAc)_2 \cdot H_2O$ (30 mg, 0.15 mmol) was dissolved in methanol (5 mL) and added to a solution of pypapn (50 mg, 0.15 mmol) in methanol (2 mL). After stirring the reaction mixture for 1 h at room temperature, $NaClO_4.H_2O$ (42 mg, 0.30 mmol) in methanol (1 mL) was added. Then, the formed solid was filtered off; hexane was added to the filtrate, and the mixture was left at 4 °C overnight. The solid was filtered, washed with cold methanol and hexane, and dried under a vacuum. Yield: 36 mg (0.06 mmol, 40%). Anal. calcd. for $C_{21}Cl_2CuH_{24}N_4O_8$: C 42.4; H 4.03; N 9.40%. Found: C 42.8; H 4.21; N 9.34%. UV-vis, λmax nm (ε M^{-1} cm^{-1}) in acetonitrile: 258 (7600); 280 (sh); 384 (sh); 653 (76). Significant IR bands (KBr, v, cm^{-1}): 3262; 2117; 1611; 1574; 1445; 1118; 622. HRMS (acetonitrile): m/z = 494.0786 [Cu(pypapn)(ClO_4)]$^+$; 395.1297 [Cu(pypapn)]$^+$. Violet crystals suitable for X-ray diffraction were obtained after 3 days by slow diffusion of the reaction of mother liquor into toluene at 4 °C.

Caution! *The perchlorate salts used in this study are potentially explosive and should be handled with care.*

3.1.2. Synthesis of Azidopropyl Functionalized Silicas N_3pn@SBA-15 and N_3pn@OP-MS

A high surface area SBA-15 mesoporous silica was prepared by hydrothermal synthesis, using tetraethoxysilane (TEOS) as Si source and the triblock copolymer Pluronic 123 as template in acid medium, as already reported [11]. The azido-functionalized N_3pn@SBA-15 silica was prepared to employ a post-synthetic approach [28] by treating a suspension of 1 g of SBA-15 silica in 30 mL of toluene with 136 mL of 3-(bromopropyl)trichlorosilane, added dropwise, and left stirring for 2 h at 80 °C. The solid was separated by filtration and washed with toluene and ether; then, Soxhlet was extracted with dichloromethane and dried under vacuum at 60 °C. Afterward, the solid was mixed with a saturated solution of NaN_3 in dimethylformamide (10.0 mL) and stirred for 2 days. After filtration, the solid was washed with water, acetone, and ethanol and dried at 60 °C to yield 0.95 g of N_3pn@SBA-15. Residual mass (%) at 800 °C: 82.5%. IR (KBr): $\nu_{as}(N_3)$ = 2114 cm^{-1}.

The one-pot azido-functionalized mesoporous silica N_3pn@OP-MS was prepared by co-condensation of TEOS (2.2 mL) and 3-azidopropyltriethoxysilane (AzPTES, 275 mg) with Pluronic P-123 (1.0 g in 40 mL of aqueous 1.6 M HCl) as surfactant template, following a previously reported methodology [28]. After the template removal by Soxhlet extraction in ethanol, the material was dried at 60 °C to yield 1.1 g of N_3pn@OP-MS. Residual mass (%) at 800 °C: 85.3%. IR (KBr): $\nu_{as}(N_3)$ = 2114 cm^{-1}.

3.1.3. Synthesis of Cu-Pypntriazole@SBA-15 and Cu-Pypntriazole@OP-MS

Azide-functionalized mesoporous silicas (350 mg) were suspended in 72 mL of a 75:25 methanol:acetonitrile mixture and stirred for ten minutes. A solution of pypapn in the same solvent mixture (30 mg, 0.09 mmol, 9 mL) was added, and the reaction mixture was stirred for 1 h. Afterward, $CuBr(PPh_3)_3$ (84 mg, 0.09 mol) was added and left with stirring at 60 °C. The completion of the reaction was determined by the disappearance of the azide stretching band at 2114 cm^{-1} in the IR spectrum. The solid, pypntriazole@SBA-15 or pypntriazole@OP-MS, was filtered, washed by Soxhlet extraction with methanol, and dried at 60 °C. Then, 250 mg of pypntriazole@SBA-15 was suspended in 25 mL methanol, and a solution of $Cu(ClO_4)_2 \cdot 6H_2O$ (300 mg, 0.8 mmol) in 5 mL of methanol was added dropwise. The mixture was stirred for one week at room temperature. The solid was filtered, washed with methanol and dichloromethane, and dried at 60 °C to yield 220 mg of Cu-pypntriazole@SBA-15. Anal. (wt.%): N 2.35; Cu 1.5. Catalyst content: 24 mmol/100g. Significant IR bands (KBr, ν cm^{-1}): 1640 (d, H-O-H); 1080 (ν_{as}, Si-O); 795 (ν_s, Si-O); 463 (δ, Si-O-Si). Following the same procedure, 250 mg of pypntriazole@OP-MS yielded 230 mg of Cu-pypntriazole@OP-MS. Anal. (wt.%): N 1.8; Cu 1.15. Catalyst content: 18 mmol/100g. Significant IR bands (KBr, ν cm^{-1}): 1640 (δ, H-O-H); 1080 (ν_{as}, Si-O); 795 (ν_s, Si-O); 463 (δ, Si-O-Si).

3.1.4. Synthesis of Encapsulated Catalyst Cu-py_2pn@SBA-15

Complex [Cu(py_2pn)(ClO_4)$_2$] was inserted in mesoporous silica SBA-15 by the addition of a solution of the complex (100 mg, 0.19 mmol) in methanol (20 mL, 35 °C) to the silica (168 mg). The mixture was stirred for 24 h and filtered. The obtained material was suspended in 5 mL of methanol and left stirring for 24 h. The solid was filtered, washed with methanol, and dried at 60 °C. Yield: 140 mg. Weight loss between 200 and 500 °C: 3.9%. Anal. (wt.%): N 0.55, Cu 0.6. Catalyst content: 9.8 mmol/100g.

3.2. Analytical and Physical Measurements

An inductively coupled plasma mass spectrometer (ICP-MS) PerkinElmer NexION 350× was used to measure the metal content. CHN analyses were performed on a PerkinElmer 2400 series II Analyzer. Infrared spectra were recorded in the 4000–400 cm^{-1} range on a PerkinElmer Spectrum One FTIR spectrophotometer provided with a DTGS detector, resolution = 4 cm^{-1}, and 10 accumulations. FT-IR spectra were registered from KBr sample pellets or ATR-FT-IR. Electronic spectra were recorded on a Jasco V-550 spectrophotometer. Electron Paramagnetic Resonance (EPR) spectra were obtained at 115 K on an Elexsys E 500 Bruker spectrometer, operating at a microwave frequency of ~9.5 GHz, and on a Bruker EMX-Plus spectrometer with a microwave frequency of ~9.3 GHz. Electrospray ionization (ESI) mass spectra were obtained with a Thermo Scientific LCQ Fleet. The solutions for electrospray were prepared from solutions of complex diluted with acetonitrile to a final ~10^{-5} M concentration. ^{1}H NMR spectra were recorded in CD_3CN on a Bruker AC 400 NMR spectrometer at ambient probe temperature (ca. 25 °C). Chemical shifts (in ppm) are referenced to tetramethylsilane, and paramagnetic NMR spectra were acquired, employing a superWEFT sequence, with an acquisition time of 270 ms. Conductivity measurements were performed on 1.0 mM solutions of the complexes in MeCN or DMF using a Horiba F-54 BW conductivity meter. The electrochemical experiments were performed with a Princeton Applied Research potentiostat, VERSASTAT II model, with the 270/250 Research Electrochemistry Software. Studies were carried out under Ar in MeCN solution using 0.1 M Bu_4NBF_4 as a supporting electrolyte and $\approx 10^{-3}$ M of the complex. The working electrode was a glassy carbon disk, and the reference electrode was a calomel electrode isolated in a fritted bridge with a Pt wire as the auxiliary electrode. Under these conditions, E(ferrocene/ferrocenium) = 388 mV in MeCN at room temperature. The size and morphology of the solid materials were analyzed using an AMR 1000 Leitz scanning electron microscope (SEM) operated at variable accelerating voltages and with EDX detector NORAN System SIX NSS-200. Samples for SEM observation were prepared by dispersing a small amount of powder of dry silica and hybrid samples on double-sided conductive adhesive tabs on top of the SEM sample holders. Then, the samples were covered by a thin layer of gold deposited by sputtering to avoid charge accumulation on the surfaces. The selected accelerating voltage used in the showed images were 20 kV at high vacuum condition. Transmission electron microscopy (TEM) analysis was performed with a TEM/STEM JEM 2100 Plus with the operational voltage of 200 kV (variable), with a LaB6 filament. The samples were prepared by dropping a suspension of material in ethanol over a Formvar/Carbon square mesh Cu, 400 Mesh grids, and let dry. TEM images were processed using the public domain ImageJ program. N_2 adsorption–desorption isotherms were obtained at 77 K on a Micrometric ASAP 2020 V4.02 (V4.02 G) apparatus. The samples were degassed at 10^{-3} Torr and 200 °C for 6 h prior to the adsorption experiment. Surface area (SBET) was calculated using the Brunauer–Emmett–Teller (BET) [55] equation over the pressure range (p/p°) of 0.05–0.20. The volume of micropores and mesopores ($V_{\mu P}$ and V_{MP}) was determined by the alpha-plot method using the standard Licrospher isotherm. The total pore volume (V_{TP}) was determined with the Gurvich rule [55] at 0.98 p/p°. The pore size distributions were calculated using the Villarroel–Bezerra–Sapag (VBS) model [56] on the desorption branch of the N_2 isotherms.

3.3. Crystal Data Collection and Refinement

Crystallographic data for compound [Cu(pypan)(ClO_4)$_2$] were collected at 298(2) K on a Bruker D8 QUEST ECO Photon II CPAD Diffractometer, using graphite monochromated Mo-Kα radiation (λ = 0.71073 Å). Data collection was carried out using the Bruker APEX4 package [57], and cell refinement and data reduction were achieved with the program SAINT V8.40B [58]. The structure was solved by direct methods with SHELXT V 2018/2 [59] and refined by full-matrix least-squares on F^2 data with SHELXL-2019/1 [60]. Molecular graphics were performed with ORTEP-3 [61], with 50% probability displacement ellipsoids. The packing diagrams were generated with SHELXL-2019/1. CCDC-2297367 contains the supplementary crystallographic data for this paper. These data can be obtained free of charge via http://www.ccdc.cam.ac.uk/conts/retrieving.html, accessed on 6 October 2023 (or from the CCDC, 12 Union Road, Cambridge CB2 1EZ, UK; Fax: +44 1223 336033; E-mail: deposit@ccdc.cam.ac.uk).

3.4. Indirect SOD Assay

An indirect assay based on the inhibition of the photoreduction of nitro blue tetrazolium (NBT) was used to test the SOD activity of the free and immobilized complexes [47]. The reaction mixture (3.2 mL) containing riboflavin (3.35 µM), methionine (9.52 mM), NBT (38.2 µM), and different amounts of free or immobilized complex was prepared in phosphate buffer of pH 7.8. Riboflavin was added last, and the mixture was illuminated for 15 min with a 16 W led lamp placed at 30 cm, at 25 °C. The reduction of NBT was measured at 560 nm. Control reactions were performed to verify that the complexes did not react with NBT or riboflavin directly. Inhibition percentage (IC) was calculated according to

$$IC = \frac{\left[(\Delta Abs/t)_{\text{without catalyst}} - (\Delta Abs/t)_{\text{with catalyst}}\right] \times 100}{(\Delta Abs/t)_{\text{without catalyst}}} \quad (1)$$

The IC_{50} values were determined from plots of % inhibition vs. complex concentration and used to calculate the McCord–Fridovich second-order rate constant (k_{McF}) [48]. At 50% inhibition, the rates of the reactions of $O_2^{\bullet -}$ with NBT and the mimic are identical; therefore, k_{McF} was calculated according to the equation k_{McF} [complex] = k_{NBT} [NBT], with k_{NBT} (pH = 7.8) = 5.94 × 10^4 M^{-1} s^{-1}.

3.5. Preparation of Potassium Superoxide Solutions

The stock solution of KO_2 in anhydrous dimethylsulfoxide (DMSO) employed in EPR measurements was prepared by suspending 9.3 mg of KO_2 in 5 mL of DMSO, followed by sonication during 15 min and centrifugation at 6000 rpm for 25 min. The concentration of KO_2 in the supernatant was calculated using ε = 2686 M^{-1} cm^{-1} in deoxygenated DMSO [62] and confirmed by the assay of the horseradish peroxidase. The saturated KO_2 solution in DMSO (0.75 mL) was added to a suspension of 10 mg of the hybrid material in 1.25 mL of DMSO, and the mixture was left stirring for 10 min. The solid was separated by centrifugation, washed with methanol, and dried at 60 °C.

4. Conclusions

[Cu(pypapn)]$^{2+}$ is among the most active Cu(II) complexes formed with open-chain ligands for catalyzing $O_2^{\bullet -}$ dismutation. In this complex, the metal ion is in a tetragonal $N_{2(amine)}N_{2(py)}O_{2(solvent)}$ environment, with the ligand disposed in the equatorial plane and two labile *trans*-positions for reaction with the substrate. The ligand flexibility seems to play a decisive role in the SOD activity, more than the redox potential, as [Cu(pypapn)]$^{2+}$ exhibits higher activity than [Cu(py_2pn)]$^{2+}$, with redox potential closer to the optimum value for $O_2^{\bullet -}$ dismutation but less conformational flexibility in the chelate rings, while displaying lower activity than complexes with a longer, and more flexible, central chain between the *N*-donor sites. Covalently linked [Cu(pypapn)]$^{2+}$ holds the metal ion geometry inside the

pores of the silica matrix and retains the SOD activity exhibited in the homogeneous phase. The silica matrix preserves its ordered mesostructure after functionalization and in the same way as the protein framework, isolates and protects the catalyst from hydrolysis, extending its lifetime. In the hybrid material obtained by encapsulation of $[Cu(py_2pn)]^{2+}$, the strong electrostatic interactions between the dicationic catalyst and the surface groups on the pores proved decisive for the full retention of the complex within the silica matrix and activation of the metal center to react with $O_2^{\bullet -}$. In view of the robustness and stability of Cu-pypntriazole@SBA-15, Cu-pypntriazole@OP-MS, and Cu-py_2pn@SBA-15, covalent anchoring and electrostatically-driven encapsulation of doubly charged copper complexes, appear suitable strategies for the design of copper-based hybrid catalysts for $O_2^{\bullet -}$ dismutation under physiological conditions.

Supplementary Materials: The following supporting information can be downloaded at https://www.mdpi.com/article/10.3390/inorganics11110425/s1, Table S1: Crystal data and structure refinement for $[Cu(pypapn)(ClO_4)_2]$; Figure S1: Crystal packing diagram for $[Cu(pypapn)(ClO_4)_2]$; Figure S2: HRMS of $[Cy(pypapn)(ClO_4)_2]$ in acetonitrile; Figure S3: Electronic spectrum of $[Cu(pypapn)(ClO_4)_2]$ in DMF; Figure S4: SEM images of the mesoporous silica and the hybrid materials; Figure S5: Histograms of the channel diameter and wall thickness of Cu-pypntriazole@SBA-15; Figure S6: Low angle X-Ray diffractograms of SBA-15 and Cu-pypntriazole@SBA-15; Chart S1: Structures of complexes listed in Table 2.

Author Contributions: Conceptualization, S.R.S. and C.P.; methodology, resources, funding acquisition, S.R.S., C.P., N.P. and C.H.; investigation, M.R., J.F., S.S., G.T., C.P. and N.P.; formal analysis, M.R., S.S., J.F., G.T., S.R.S. and N.P.; writing—original draft preparation, S.R.S.; writing—review and editing, S.R.S., C.H., N.P. and C.P.; supervision, S.R.S. and C.P. All authors have read and agreed to the published version of the manuscript.

Funding: This research was funded by National University of Rosario (PID 80020220700136UR and PID 8002019040023UR), Consejo Nacional de Investigaciones Científicas y Técnicas (CONICET, PIP-0852 and PUE-0068), Centre National de la Recherche Scientifique (CNRS, PICS-07121), and Agencia Nacional de Promoción Científica y Tecnológica (ANPCyT, PICT-2019-03276).

Data Availability Statement: The data presented in this study are available on request from the corresponding author.

Conflicts of Interest: The authors declare no conflict of interest. The funders had no role in the design of this study.

References

1. Yang, B.; Chen, Y.; Shi, J. Reactive Oxygen Species (ROS)-Based Nanomedicine. *Chem. Rev.* **2019**, *119*, 4881–4985. [CrossRef] [PubMed]
2. Abreu, I.A.; Cabelli, D.E. Superoxide dismutases—A review of the metal-associated mechanistic variations. *Biochim. Biophys. Acta* **2010**, *1804*, 263–274. [CrossRef]
3. Batinić-Haberle, I.; Reboucas, J.S.; Spasojević, I. Superoxide dismutase mimics: Chemistry, pharmacology, and therapeutic potential. *Antioxid. Redox. Signal.* **2010**, *13*, 877–918. [CrossRef]
4. Riley, D.P. Functional Mimics of Superoxide Dismutase Enzymes as Therapeutic Agents. *Chem. Rev.* **1999**, *99*, 2573–2587. [CrossRef]
5. Sheng, Y.; Abreu, I.A.; Cabelli, D.E.; Maroney, M.J.; Miller, A.-F.; Teixeira, M.; Valentine, J.S. Superoxide Dismutases and Superoxide Reductases. *Chem. Rev.* **2014**, *114*, 3854–3918. [CrossRef]
6. Tainer, J.A.; Getzoff, E.D.; Beem, K.M.; Richardson, J.S.; Richardson, D.C. Determination and analysis of the 2 Å structure of copper, zinc superoxide dismutase. *J. Mol. Biol.* **1982**, *160*, 181–217. [CrossRef]
7. Richezzi, M.; Ferreyra, J.; Puzzolo, J.; Milesi, L.; Palopoli, C.M.; Moreno, D.M.; Hureau, C.; Signorella, S.R. Versatile Activity of a Copper(II) Complex Bearing a N_4-Tetradentate Schiff Base Ligand with Reduced Oxygen Species. *Eur. J. Inorg. Chem.* **2022**, *2022*, e202101042. [CrossRef]
8. Lange, J.; Elias, H.; Paulus, H.; Müller, J.; Weser, U. Copper(II) and Copper(I) complexes with an open-chain N_4 Schiff base ligand modeling CuZn superoxide dismutase: Structural and spectroscopic characterization and kinetics of electron transfer. *Inorg. Chem.* **2000**, *39*, 3342–3349. [CrossRef] [PubMed]
9. Müller, J.; Felix, K.; Maichle, C.; Lengfelder, E.; Strähle, J.; Weser, U. Phenyl-Substituted Copper Di-Schiff Base, a Potent CuZn Superoxide Dismutase Mimic Surviving Competitive Biochelation. *Inorg. Chim. Acta* **1995**, *233*, 11–19. [CrossRef]

10. Pap, J.S.; Kripli, B.; Bors, I.; Bogáth, D.; Giorgi, M.; Kaizer, J.; Speier, G. Transition Metal Complexes Bearing Flexible N_3 or N_3O Donor Ligands: Reactivity toward Superoxide Radical Anion and Hydrogen Peroxide. *J. Inorg. Biochem.* **2012**, *117*, 60–70. [CrossRef]
11. Patriarca, M.; Daier, V.; Camí, G.; Pellegri, N.; Rivière, E.; Hureau, C.; Signorella, S. Biomimetic Cu, Zn and Cu_2 Complexes Inserted in Mesoporous Silica as Catalysts for Superoxide Dismutation. *Microporous Mesoporous Mater.* **2019**, *279*, 133–141. [CrossRef]
12. Müller, J.; Schübl, D.; Maichle-Mössmer, C.; Strähle, J.; Weser, U. Structure—Function Correlation of Cu (II)-and Cu (I)-Di-Schiff-Base Complexes during the Catalysis of Superoxide Dismutation. *J. Inorg. Biochem.* **1999**, *75*, 63–69. [CrossRef]
13. Ribeiro, T.P.; Fernandes, C.; Melo, K.V.; Ferreira, S.S.; Lessa, J.A.; Franco, R.W.A.; Schenk, G.; Pereira, M.D.; Horn, A., Jr. Iron, Copper, and Manganese Complexes with in Vitro Superoxide Dismutase and/or Catalase Activities That Keep Saccharomyces Cerevisiae Cells Alive under Severe Oxidative Stress. *Free Radic. Biol. Med.* **2015**, *80*, 67–76. [CrossRef]
14. Mekhail, M.A.; Smith, K.J.; Freire, D.M.; Pota, K.; Nguyen, N.; Burnett, M.E.; Green, K.N. Increased Efficiency of a Functional SOD Mimic Achieved with Pyridine Modification on a Pyclen-Based Copper(II) Complex. *Inorg. Chem.* **2023**, *62*, 5415–5425. [CrossRef]
15. Green, K.N.; Pota, K.; Tircso, G.; Gogolak, R.A.; Kinsinger, O.; Davda, C.; Blain, K.; Brewer, S.M.; Gonzalez, P.; Johnston, H.M.; et al. Dialing in on pharmacological features for a therapeutic antioxidant small molecule. *Dalton Trans.* **2019**, *48*, 12430–12439. [CrossRef]
16. Policar, C.; Bouvet, J.; Bertrand, H.C.; Delsuc, N. SOD mimics: From the tool box of the chemists to cellular studies. *Curr. Opin. Chem. Biol.* **2022**, *67*, 102109. [CrossRef]
17. Martinez-Camarena, Á.; Sanchez-Murcia, P.A.; Blasco, S.; Gonzalez, L.; Garcia-España, E. Unveiling the reaction mechanism of novel copper N-alkylated tetra-azacyclophanes with outstanding superoxide dismutase activity. *Chem. Commun.* **2020**, *56*, 7511–7514. [CrossRef]
18. Vaughn, B.A.; Brown, A.M.; Ahn, S.H.; Robinson, J.R.; Borosm, E. Is Less More? Influence of the Coordination Geometry of Copper(II)Picolinate Chelate Complexes on Metabolic Stability. *Inorg. Chem.* **2020**, *59*, 16095–16108. [CrossRef]
19. Smits, N.W.G.; van Dijk, B.; de Bruin, I.; Groeneveld, S.L.T.; Siegler, M.A.; Hetterscheid, D.G.H. Influence of Ligand Denticity and Flexibility on the Molecular Copper Mediated Oxygen Reduction Reaction. *Inorg. Chem.* **2020**, *59*, 16398–16409. [CrossRef]
20. Stanek, J.; Hoffmann, A.; Herres-Pawlis, S. Renaissance of the entatic state principle. *Coord. Chem. Rev.* **2018**, *365*, 103–121. [CrossRef]
21. Falcone, E.; Hureau, C. Redox processes in Cu-binding proteins: The "in-between" states in intrinsically disordered peptides. *Chem. Soc. Rev.* **2023**, *52*, 6595–6600. [CrossRef]
22. Uzal-Varela, R.; Patinec, V.; Tripier, R.; Valencia, L.; Maneiro, M.; Canle, M.; Platas-Iglesias, C.; Esteban-Gómez, D.; Iglesias, E. On the dissociation pathways of copper complexes relevant as PET imaging agents. *J. Inorg. Biochem.* **2022**, *236*, 111951. [CrossRef]
23. Mohammadnezhad, G.; Amirian, A.M.; Plass, H.G.W.; Sandleben, A.; Schäfer, S.; Klein, A. Redox Instability of Copper(II) Complexes of a Triazine-Based PNP Pincer. *Eur. J. Inorg. Chem.* **2021**, *2021*, 1140–1151. [CrossRef]
24. Mureseanu, M.; Filip, M.; Bleotu, I.; Spinu, C.I.; Marin, A.H.; Matei, I.; Parvulescu, V. Cu(II) and Mn(II) Anchored on Functionalized Mesoporous Silica with Schiff Bases: Effects of Supports and Metal–Ligand Interactions on Catalytic Activity. *Nanomaterials* **2023**, *13*, 1884. [CrossRef]
25. Isa, E.D.M.; Ahmad, H.; Rahman, M.B.A.; Gill, M.R. Progress in Mesoporous Silica Nanoparticles as Drug Delivery Agents for Cancer Treatment. *Pharmaceutics* **2021**, *13*, 152.
26. Cadavid-Vargas, J.F.; Arnal, P.M.; Sepúlveda, R.D.M.; Rizzo, A.; Soria, D.B.; Di Virgilio, A.L. Copper complex with sulfamethazine and 2,2′-bipyridine supported on mesoporous silica microspheres improves its antitumor action toward human osteosarcoma cells: Cyto- and genotoxic effects. *Biometals* **2019**, *32*, 21–32. [CrossRef]
27. Donato, L.; Atoini, Y.; Prasetyanto, E.A.; Chen, P.; Rosticher, C.; Bizarri, C.; Rissansen, K.; De Cola, L. Selective encapsulation and enhancement of the emission properties of a luminescent Cu(I) complex in mesoporous silica. *Helvetica Chim. Acta* **2018**, *101*, e1700273. [CrossRef]
28. Richezzi, M.; Palopoli, C.; Pellegri, N.; Hureau, C.; Signorella, S.R. Synthesis, characterization and superoxide dismutase activity of a biomimetic Mn(III) complex covalently anchored to mesoporous silica. *J. Inorg. Biochem.* **2022**, *237*, 112026. [CrossRef] [PubMed]
29. Pajchel, L.; Kolodziejski, W. Synthesis and characterization of MCM-48/hydroxyapatite composites for drug delivery: Ibuprofen incorporation, location and release studies. *Mater. Sci. Eng. C* **2018**, *91*, 734–742. [CrossRef] [PubMed]
30. Lu, Z.; Wang, J.; Qu, L.; Kan, G.; Zhang, T.; Shen, J.; Li, Y.; Yang, J.; Niu, Y.; Xiao, Z.; et al. Reactive mesoporous silica nanoparticles loaded with limonene for improving physical and mental health of mice at simulated microgravity condition. *Bioact. Mater.* **2020**, *5*, 1127–1137. [CrossRef]
31. Wang, L.S.; Wu, L.C.; Lu, S.Y.; Chang, L.L.; Teng, I.T.; Yang, C.M.; Ho, J.A. Biofunctionalized Phospholipid-Capped Mesoporous Silica Nanoshuttles for Targeted Drug Delivery: Improved Water Suspensibility and Decreased Nonspecific Protein Binding. *ACS Nano* **2010**, *4*, 4371–4379. [CrossRef]
32. Martinez-Carmona, M.; Lozano, D.; Colilla, M.; Vallet-Regí, M. Lectin-conjugated pH-responsive mesoporous silica nanoparticles for targeted bone cancer treatment. *Acta Biomater.* **2018**, *65*, 393–404. [CrossRef]
33. Ha, S.W.; Viggeswarapu, M.; Habib, M.M.; Beck, G.R., Jr. Bioactive effects of silica nanoparticles on bone cells are size, surface, and composition dependent. *Acta Biomater.* **2018**, *82*, 184–196. [CrossRef]

34. Zhao, N.; Yan, L.; Zhao, X.; Chen, X.; Li, A.; Zheng, D.; Zhou, X.; Dai, X.; Xu, F.J. Versatile Types of Organic/Inorganic Nanohybrids: From Strategic Design to Biomedical Applications. *Chem. Rev.* **2019**, *119*, 1666–1762. [CrossRef]
35. Freire, C.; Pereira, C.; Rebelo, S. Green oxidation catalysis with metal complexes: From bulk to nano recyclable hybrid catalysts. *Catalysis* **2012**, *24*, 116–203.
36. Rana, B.S.; Jain, S.L.; Singh, B.; Bhaumik, A.; Sain, B.; Sinha, A.K. Click on silica: Systematic immobilization of Co(II)Schiff bases to the mesoporous silicavia click reaction and their catalytic activity for aerobic oxidation of alcohols. *Dalton Trans.* **2010**, *39*, 7760–7767. [CrossRef]
37. Bagherzadeh, M.; Hosseini, M.; Mortazavi-Manesh, A. Manganese(III) porphyrin anchored onto magnetic nanoparticles via "Click" reaction: An efficient and reusable catalyst for the heterogeneous oxidation of alkenes and sulfides. *Inorg. Chem. Commun.* **2019**, *107*, 107495. [CrossRef]
38. Richezzi, M.; Signorella, S.; Palopoli, C.; Pellegri, N.; Hureau, C.; Signorella, S.R. The Critical Role of Ligand Flexibility on the Activity of Free and Immobilized Mn Superoxide Dismutase Mimics. *Inorganics* **2023**, *11*, 359. [CrossRef]
39. Pat McCurdie, M.; Belfiore, L.A. Spectroscopic analysis of transition-metal coordination complexes based on poly(4-vinylpyridine) and dichlorotricarbonylruthenium(II). *Polymer* **1999**, *40*, 2889–2902. [CrossRef]
40. Subramanian, P.S.; Suresh, E.; Dastidar, P.; Waghmode, S.; Srinivas, D. Conformational Isomerism and Weak Molecular and Magnetic Interactions in Ternary Copper(II) Complexes of $[Cu(AA)L']ClO_4 \cdot nH_2O$, Where AA = L-Phenylalanine and L-Histidine, L′ = 1,10-Phenanthroline and 2,2-Bipyridine, and n = 1 or 1.5: Synthesis, Single-Crystal X-ray Structures, and Magnetic Resonance Investigations. *Inorg. Chem.* **2001**, *40*, 4291–4301.
41. Muthuramalingam, S.; Anandababu, K.; Velusamy, M.; Mayilmurugan, R. Benzene Hydroxylation by Bioinspired Copper(II) Complexes: Coordination Geometry versus Reactivity. *Inorg. Chem.* **2020**, *59*, 5918–5928. [CrossRef]
42. Geary, W.J. The use of conductivity measurements in organic solvents for the characterization of coordination compounds. *Coord. Chem. Rev.* **1971**, *7*, 81–122. [CrossRef]
43. Malvi, B.; Sarkar, B.R.; Pati, D.; Mathew, R.; Ajithkumarb, T.G.; Sen Gupta, S. "Clickable" SBA-15 mesoporous materials: Synthesis, characterization and their reaction with alkynes. *J. Mater. Chem.* **2009**, *19*, 1409–1416. [CrossRef]
44. Mercier, L.; Pinnavaia, T.J. Direct Synthesis of Hybrid Organic-Inorganic Nanoporous Silica by a Neutral Amine Assembly Route: Structure-Function Control by Stoichiometric Incorporation of Organosiloxane Molecules. *Chem. Mater.* **2000**, *12*, 188–196. [CrossRef]
45. Zhao, D.; Feng, J.; Huo, Q.; Melosh, N.; Frederichson, G.H.; Chmelka, B.F.; Stucky, G.D. Triblock Copolymer Syntheses of Mesoporous Silica with Periodic 50 to 300 Angstrom Pores. *Science* **1998**, *279*, 548–552. [CrossRef]
46. Taghavimoghaddam, J.; Knowles, G.P.; Chaffee, A.L. SBA-15 supported cobalt oxide species: Synthesis, morphology and catalytic oxidation of cyclohexanol using TBHP. *J. Mol. Catal. A Chem.* **2013**, *379*, 277–286. [CrossRef]
47. Beauchamps, C.; Fridovich, I. Superoxide dismutase: Improved assays and an assay applicable to acrylamide gels. *Anal. Biochem.* **1971**, *44*, 276–287. [CrossRef]
48. Liao, Z.-R.; Zheng, X.-F.; Luo, B.-S.; Shen, L.-R.; Li, D.-F.; Liu, H.-L.; Zhao, W. SOD-like activities of manganese-containing complexes with N,N,N,N-tetrakis(2-benzimidazolyl methyl)-1,2-ethanediamine (EDTB). *Polyhedron* **2001**, *20*, 2813–2821. [CrossRef]
49. Wang, C.; Li, S.; Shang, D.-J.; Wang, X.-L.; You, Z.-L.; Li, H.-B. Antihyperglycemic and neuroprotective effects of one novel Cu–Zn SOD mimetic. *Bioorg. Med. Chem. Lett.* **2011**, *21*, 4320–4324. [CrossRef]
50. You, Z.-L.; Ni, L.-L.; Hou, P.; Zhang, J.-C.; Wang, C. Synthesis, Crystal Structures, and Superoxide Dismutase Activity of Two Isostructural Copper(II)—Zinc(II) Complexes Derived from N,N′-Bis (4-Methoxysalicylidene) Cyclohexane-1, 2-Diamine. *J. Coord. Chem.* **2010**, *63*, 515–523. [CrossRef]
51. Ivanović-Burmazović, I.; Filipović, M.R. Chapter 3—Reactivity of manganese superoxide dismutase mimics toward superoxide and nitric oxide: Selectivity versus cross-reactivity. *Adv. Inorg. Chem.* **2012**, *64*, 53–95.
52. Diószegi, R.; Bonczidai-Kelemen, D.; Bényei, A.C.; May, N.V.; Fábián, I.; Lihi, N. Copper(II) Complexes of Pyridine-2,6-dicarboxamide Ligands with High SOD Activity. *Inorg. Chem.* **2022**, *61*, 2319–2332. [CrossRef]
53. Bagchi, R.N.; Bond, A.M.; Scholz, F.; Stösser, R. Characterization of the ESR spectrum of the superoxide anion in the liquid phase. *J. Am. Chem. Soc.* **1989**, *111*, 8270–8271. [CrossRef]
54. Ebralidze, I.I.; Leitus, G.; Shimon, L.J.W.; Wang, Y.; Shaik, S.; Neumann, R. Structural variability in manganese(II) complexes of N,N′-bis(2-pyridinylmethylene) ethane (and propane) diamine ligands. *Inorg. Chim. Acta* **2009**, *362*, 4713–4720. [CrossRef]
55. Thommes, M.; Kaneko, K.; Neimark, A.V.; Olivier, J.P.; Rodriguez-Reinoso, F.; Rouquerol, J.; Sing, K.S.W. Physisorption of gases, with special reference to the evaluation of surface area and pore size distribution (IUPAC Technical Report). *Pure Appl. Chem.* **2015**, *87*, 1051–1069. [CrossRef]
56. Villarroel Rocha, J.; Barrera, D.; Sapag, K. Improvement in the Pore Size Distribution for Ordered Mesoporous Materials with Cylindrical and Spherical Pores Using the Kelvin Equation. *Top. Catal.* **2011**, *54*, 121–134. [CrossRef]
57. *Bruker*, APEX4 v2022.10-1; Bruker AXS Inc.: Madison, WI, USA, 2022.
58. *Bruker*, SAINT V8.40B; Bruker AXS Inc.: Madison, WI, USA, 2019.
59. Sheldrick, G.M. SHELXT-Integrated space-group and crystal-structure determination. *Acta Cryst.* **2015**, *A71*, 3–8. [CrossRef]
60. Sheldrick, G.M. Crystal structure refinement with SHELXL. *Acta Cryst.* **2015**, *C71*, 3–8.

61. Farrugia, L.J. ORTEP3 for Windows. *J. Appl. Crystallogr.* **1997**, *30*, 565. [CrossRef]
62. Hyland, K.; Auclair, C. The formation of superoxide radical anions by a reaction between O_2, OH^- and dimethyl sulfoxide. *Biochem. Biophys. Res. Commun.* **1981**, *102*, 531–537. [CrossRef]